

QUANTITATIVE MOBILITY SPECTRUM ANALYSIS
OF III-V HETEROSTRUCTURES ON SILICON

THESIS

Presented to the Graduate Council of
Texas State University-San Marcos
in Partial Fulfillment
of the Requirements

for the Degree

Master of SCIENCE

by

Thiess H. Cunningham, B.S.

San Marcos, Texas
December 2012

QUANTITATIVE MOBILITY SPECTRUM ANALYSIS
OF III-V HETEROSTRUCTURES ON SILICON

Committee Members Approved:

Ravindranath Droopad, Chair

Man Hoi Wong

David Donnelly

Approved:

J. Michael Willoughby
Dean of the Graduate College

COPYRIGHT

by

Thiess Howard Cunningham

2012

FAIR USE AND AUTHOR'S PERMISSION STATEMENT

Fair Use

This work is protected by the Copyright Laws of the United States (Public Law 94-553, section 107). Consistent with fair use as defined in the Copyright Laws, brief quotations from this material are allowed with proper acknowledgment. Use of this material for financial gain without the author's express written permission is not allowed.

Duplication Permission

As the copyright holder of this work I, Thiess Howard Cunningham, authorize duplication of this work, in whole or in part, for educational or scholarly purposes only.

DEDICATION

All of my work is dedicated to my wife Tamara Cunningham for her love, relentless support and understanding throughout my education; including through my bachelor's whilst working nights and up through my master's when I was away studying for so many hours!

ACKNOWLEDGEMENTS

I would like to thank my thesis committee advisor Ravi Droopad for the 18 months of guidance, encouragement and challenges and his knowledge on MBE cannot be overlooked. Also I would like to thank Richard Hill my internship sponsor for his knowledge of device integration and understanding. Thanks to Man Hoi for his endless willingness to supply me with resources and knowledge of MBE, QMSA, & XRD.

Thanks to Craig Swartz for teaching me the inner workings of the PPMS and about QMSA.. He always found time to help me with QMSA and never left without teaching me something. Thanks to Albert Wang for his help with Hall, VDP and QMSA. Thanks to Rocio Contreras for teaching me so much about MBE.

Finally I would like to thank my parents Kent and Dayna Cunningham, sister and her husband Traci and Eric Schulte, and my parent-in-laws Jamie and Paula McClanahan for the support, faith, encouragement, and love throughout my life to graduation.

This manuscript was submitted on November 5, 2012.

TABLE OF CONTENTS

ACKNOWLEDGMENTS	vi
LIST OF FIGURES	ix
ABSTRACT.....	xi
CHAPTER	
I. INTRODUCTION	1
Why III-V Materials?	2
Why Silicon?.....	2
II. QUANTITATIVE MOBILITY SPECTRUM ANALYSIS.....	4
Introduction.....	4
The Hall Effect.....	5
The Van der Pauw Technique.....	9
The Hall Effect Measurement.....	15
Theory of QMSA	16
Advantages of QMSA.....	20
III. MOLECULAR BEAM EPITAXY	22
Introduction.....	22
Theory of MBE	23
Advantages of MBE.....	25
Heterostructures	26
IV. QMSA EQUIPMENT & PROCEDURES.....	29
Physical Property Measurement System.....	29
QMSA.....	33
Procedure	35

V. RESULTS & DISCUSSION.....	37
Structures on Si and InP.....	37
In _{0.53} GaAs/In _{0.52} AlAs on InP and Si	41
VI. CONCLUSIONS	46
DEFINITIONS.....	47
APPENDIX.....	50
LITERATURE CITED	51
VITA.....	53

LIST OF FIGURES

Figure	Page
1: Hall Effect on holes and electrons [2]	6
2: Van Der Pauw Technique [3]	11
3: A Cross Bridge Sample.....	12
4: Preferred and Acceptable VDP Shape and Contact Configurations [3]	12
5: Correction Factor C versus d/l for contacts at the center and at the corners of the square [4]	13
6: Measurement Demo.....	14
7: Reversed Current	14
8: Remaining Six Currents.....	15
9: Calculate Resistances.....	15
10: Greek Cross Hall-Bar Configuration	18
11: Generic HEMT structure	28
12: Quantum Design PPMS Evercool Chamber	30
13: PPMS Inner Schematic [23]	31
14: CSW-71 Helium Compressor Unit.....	32
15: Quantum Design PPMS Tower	33
16: Mobility Peaks of Si-HEMT measured at 300K.....	35
17: Mobility Peaks of Si-HEMT measured at 77K.....	35
18: HEMT on InP.....	39
19: HEMT structure on Silicon.....	40

20: Cross Section TEM of HEMT-Si - x68k magnification	41
21: μ & n_s at 300K of HEMT-Si.....	44
22: μ & n_s at 300K of HEMT-InP	44
23: μ & n_s at 77K of HEMT-Si.....	44
24: μ & n_s at 77K of HEMT-InP	44
25: μ & n_s at 10K of HEMT-Si.....	44
26: μ & n_s at 10K of HEMT-InP	44
27: Mobility HEMT-Si at 300K.....	45
28: Mobility HEMT-InP at 300K	45
29: Mobility HEMT-Si at 77K.....	45
30: Mobility HEMT-InP at 77K	45
31: Mobility HEMT-Si at 10K.....	45
32: Mobility HEMT-InP at 10K	45

ABSTRACT

QUANTITATIVE MOBILITY SPECTRUM ANALYSIS OF III-V HETEROSTRUCTURES ON SILICON

by

Thiess Howard Cunningham, B.S.

Texas State University-San Marcos

December 2012

SUPERVISING PROFESSOR: RAVI DROOPAD

The continued scaling of Si CMOS devices as had been practiced by the electronics industry has reached the point where, alternative solutions to the conventional MOSFET device need to be found. There is widespread consensus that high mobility III-V channel materials with their high electron mobilities and velocities will enable increased performance and reduced power consumption at scaled geometries. While the industry is currently targeting the 11 nm technology node for their introduction, there are significant challenges remaining before high mobility materials can be adopted for high volume manufacturing (HVM). One of the requirements is that these materials need to be epitaxially integrated onto silicon and be able to withstand the processing environment in the various CMOS modules. The challenge is to characterize and eventually to minimize

the defects in these heterostructures when grown on silicon substrates due to the differences in lattice constants. Characterization of these structures is necessary to determine whether there are any roadblocks to device operation.

In this thesis, the electrical characterization of MBE grown III-V InGaAs/InAlAs heterostructures on silicon and native InP substrates using variable field Hall measurements at temperatures ranging from 10K-room temperature in magnetic fields from 0-9T will be presented. From these measurements, Quantitative Mobility Spectrum Analysis (QMSA) of the data is carried out to determine the densities and mobilities of the carriers and the effect of epitaxial defects on channel transport and buffer leakage. This data is then used for growth optimization to be able to develop material structures suitable for HVM of CMOS at the 11nm node and beyond.

I. INTRODUCTION

Future generations of complementary metal oxide semiconductor (CMOS) devices rely on the ability to continue the scaling of transistors on a silicon platform. However, the industry has reached a point in which the device properties are beginning to degrade as the device's dimensions are being reduced. As an alternative, compound semiconductors are being pursued as a solution to increase the mobility of the channel. As part of this strategy, III-V-based device structures are needed to be monolithically integrated on Silicon substrates. This thesis compares the mobility analysis of III-V heterostructures grown by molecular beam epitaxy on silicon and native InP substrates. Electrical characterization is carried out using variable-field Hall Effect measurements from 0-9 Tesla at various temperatures. The mobilities and carriers are extracted from the resistivities using Quantitative Mobility Spectrum Analysis.

The QMSA technique is based on an algorithm which optimizes a curve fitting to the conductivity tensor components and their slopes by making adjustments in the mobility spectra that result in the greatest error reduction. QMSA maximizes the information that may be extracted from a given data set; in fact it provides superior results with more data than conventional single field Hall measurements. Also QMSA is suitable for use as a standard tool in the electrical characterization of semiconductor material and device transport properties [2]. When these transport measurements are done

at a wide range of magnetic fields the advantage of QMSA is that it distinguishes between the multiple carrier mobilities that exist in the structure.

Why III-V Materials?

Among the strategies being pursued to continue the trends of performance increase and size decrease proposed by the International Technology Roadmap for Semiconductors (ITRS) is the use of III-V semiconductors as channel materials replacing the established silicon channels. With scaling, in addition to gate leakage, the mobility of the Si channel degrades and while strain has been introduced to mitigate this degradation, the need for replacing Si is becoming apparent. III-V semiconductors are a class of materials that provide much higher carrier mobilities and possess higher electron velocities which can be used in MOSFET devices with lower operating voltage and reduced power consumption.

Why Silicon?

Compound semiconductors, most notably III-V channel materials owe much of their enhanced properties to the low effective mass and direct bandgap at the Brillouin Zone center enabling high speed optoelectronic devices. For application into the ITRS roadmap, they must be implemented onto silicon to use the VLSI toolsets which account for billions of dollars' worth in capital investments in the major fabs around the world.

The heteroepitaxial integration of III-V materials onto silicon will need to overcome the lattice mismatch due to the differences in lattice constants. In addition, the growth at high temperatures will produce additional structural defects if lattice mismatch is present. The mismatch will cause lattice strain, threading dislocations, and possible antiphase domains due to the growth of polar III-V materials on non-polar silicon

substrates. These will combine to act as scattering centers for carrier transport. The need therefore is to understand the transport properties of III-V heterostructures on Si substrates and the effect of the various defects. Various deposition techniques need to be developed to allow for the reduction of these defects. A comparison with similar structures on native substrates will determine the effectiveness of the growth process. The pertinent challenges of III-V on silicon are the main focus of the industry. QMSA is unique and still being improved as a viable technique to characterize these revolutionary devices.

II. QUANTITATIVE MOBILITY SPECTRUM ANALYSIS

Introduction

Advances in compound semiconductors have resulted in novel heterostructure devices with superior performance. These devices are widely used in RF, microwave, and optical applications today. The rapid pace with which these device technologies have advanced have, in turn, necessitated the development of new measurement and data analysis techniques. For example, conventional single magnetic field Hall characterization is incapable of providing a precise determination of the electronic transport properties of a multi-layered device such as a pseudomorphic high electron mobility transistor (pHEMT) [1]. The keys to a pHEMT are the mobility and density of the two-dimensional electron gas (2DEG) carrier (or carriers) in the quantum well channel layer. To characterize this, repeated single field hall measurements are made as a function of and etching the surface layer until the doped cap layer is removed. Even when done this way the accuracy of the characterization is not guaranteed if additional carrier(s) such as surface and interface charges exist in the sample [1]. Combined conduction effects frequently dominate the magnetotransport properties of semiconductor materials, including bulk samples, thin films, quantum wells (QWs), and processed devices.

Standard single-field measurements of the resistivity and Hall coefficient are of limited use when applied to systems with prominent mixed conduction, since they

provide only averaged values of the carrier concentration and mobility, which are not necessarily representative of any of the individual species. Far more information

becomes available when magnetotransport experiments are performed as a function of magnetic field, because in principle one can then deconvolve the data to obtain densities and mobilities for each carrier present [2].

The Hall Effect

The Hall Effect theory described here will be used along with the Van der Pauw technique to provide the data that will be the backbone of the analysis of the structures.

The Hall Effect is illustrated in Figure 1. The current would flow from left to right denoted by I_x and the resultant behavior of electrons and holes due to the applied electric and magnetic fields is denoted by E_y . The resultant E_y depends on whether the sample is p-type or n-type.

$$E_y = v_x B_z = \frac{B_z J_x}{ne} = R_H J_x B_z \quad (\text{II.1})$$

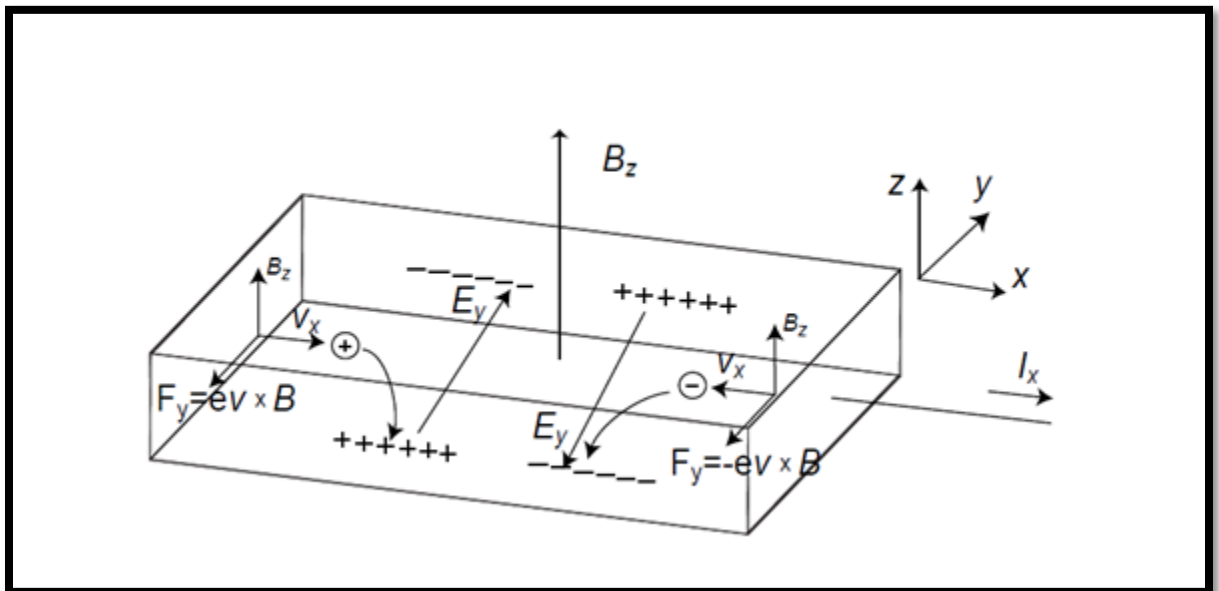


Figure 1: Hall Effect on holes and electrons [2].

The Hall Coefficient,

$$R_H = \pm \frac{1}{qn}, \quad q = 1.6 \times 10^{-19} \text{ C},$$

n is the carrier density. At the steady state, $J_y=0$. The Hall angle:

$$\tan \theta_H = \frac{E_y}{E_x} \quad (\text{II.2})$$

At low bias and constant $\mu(E)$, the velocity of electrons can be expressed by,

$$v_x = -\mu_e E_x, \quad (\text{II.3})$$

where μ_e is the electron mobility:

$$\mu_e = \frac{e\tau}{m^*}, \quad (\text{II.4})$$

where τ is the carrier relaxation time and m^* is the effective mass. The current density is calculated by,

$$J_x = ne \mu_e E_x.$$

Substitute J_x into (II.2):

$$\tan \theta_H = -\mu_e B_z = -\omega_c \tau \quad (\text{II.5})$$

Where, $\omega_c = \frac{eB_z}{m^*}$, is the cyclotron angular frequency. Note: It is assumed τ is

independent of the carrier energy, and needs the corrective Hall Scattering factor: $r_H =$

$\langle \tau^2 \rangle / \langle \tau \rangle^2$, where τ is carrier relaxation time. Thus:

$$R_H = -\frac{r_H}{ne}, \quad (\text{II.6})$$

$$R_H = \frac{r_H}{pe}, \quad (\text{II.7})$$

for electrons and holes respectively. With the conductivity, $\sigma = ne\mu$ and equations

(II.6) and (II.7) it is shown:

$$|R_H|\sigma = r_H\mu = \mu_H, \quad (\text{II.8})$$

Where μ_H is the Hall mobility. The Hall Scattering Factor depends on the type of scattering mechanism and generally falls between 1 and 2 for most semiconductors. The motion for an electron under magnetic and electric fields is written as:

$$\frac{m^* dv}{dt} + \frac{m^* v}{\tau} = -e(E + v \times B). \quad (\text{II.9})$$

In the presence of a magnetic field \mathbf{B} , the drift velocity can be expressed by:

$$v_d = -\frac{e\tau}{m^*}(E + v_c \times B) \quad (\text{II.10})$$

If the magnetic field is along the +z direction, then II.10 leads to:

$$\begin{aligned} v_x &= -\frac{e\tau}{m^*}(E_x + v_y B_z), \\ v_y &= -\frac{e\tau}{m^*}(E_y - v_x B_z), \\ v_z &= -\frac{e\tau}{m^*}(E_z). \end{aligned} \quad (\text{II.11})$$

By substituting the Hall Angle into (II.11), it is shown:

$$\begin{aligned} v_x &= -\frac{e}{m^*} \left(\frac{\tau}{1 + \omega_c^2 \tau^2} E_x - \frac{\omega_c \tau^2}{1 + \omega_c^2 \tau^2} E_y \right), \\ v_y &= -\frac{e}{m^*} \left(\frac{\omega_c \tau^2}{1 + \omega_c^2 \tau^2} E_x + \frac{\tau}{1 + \omega_c^2 \tau^2} E_y \right), \\ v_z &= -\frac{e}{m^*} \tau E_z. \end{aligned} \quad (\text{II.12})$$

The e^- current density is given by, $J = env$, so:

$$J_x = \frac{ne^2}{m^*} \left(\frac{\tau}{1 + \omega_c^2 \tau^2} E_x - \frac{\omega_c \tau^2}{1 + \omega_c^2 \tau^2} E_y \right),$$

$$J_y = \frac{ne^2}{m^*} \left(\frac{\omega_c \tau^2}{1 + \omega_c^2 \tau^2} E_x + \frac{\tau}{1 + \omega_c^2 \tau^2} E_y \right), \quad (\text{II.13})$$

$$J_z = \frac{ne^2}{m^*} \tau E_z.$$

If the current is written as:

$$J_i = \sigma_{ij} E_j, \quad (\text{II.14})$$

the conductivity can be shown as a tensor:

$$[\sigma] = \begin{bmatrix} \sigma_{xx} & \sigma_{xy} & 0 \\ \sigma_{yx} & \sigma_{yy} & 0 \\ 0 & 0 & \sigma_{zz} \end{bmatrix}, \quad (\text{II.15})$$

Where,

$$\sigma_{xx} = \sigma_{yy} = \frac{ne^2}{m^*} \frac{\tau}{1 + \omega_c^2 \tau^2}, \quad (\text{II.16})$$

$$\sigma_{xy} = -\sigma_{yx} = \frac{-ne^2}{m^*} \frac{\omega_c^2 \tau^2}{1 + \omega_c^2 \tau^2}, \quad (\text{II.17})$$

$$\sigma_{zz} = \frac{ne^2}{m^*} \tau \equiv \sigma_0. \quad (\text{II.18})$$

So the current density in x and y directions are expressed as:

$$J_x = \sigma_{xx} E_x + \sigma_{xy} E_y, \quad (\text{II.19})$$

$$J_y = \sigma_{yx} E_x + \sigma_{yy} E_y. \quad (\text{II.20})$$

The Hall Effect is measured at the steady state when $J_y=0$, so:

$$J_x = \frac{\sigma_{xx}^2 + \sigma_{xy}^2}{\sigma_{xx}} E_x = \sigma_0 E_x, \quad (\text{II.21})$$

using (II.2) and (II.17). The resistivity ρ (in the current direction) can be expressed as:

$$\rho = \frac{\sigma_{xy}}{\sigma_{xx}^2 + \sigma_{xy}^2}. \quad (\text{II.22})$$

The Hall coefficient is given by:

$$R_H = \frac{1}{B} \frac{\sigma_{xy}}{\sigma_{xx}^2 + \sigma_{xy}^2}. \quad (\text{II.23})$$

using (II.1). The result is a field-independent resistivity after assuming: isotropic effective mass, carrier relaxation time assumed to be carrier energy-independent, both holes and electrons were assumed to have equivalent velocity. Also the shape of the sample was unconsidered.

The Van der Pauw Technique

In order to determine both the mobility μ and the sheet density n_s , a combination of a resistivity measurement and a Hall Effect measurement is needed. The Van der Pauw (VDP) technique due to its convenience is widely used in the semiconductor industry to determine the resistivity of uniform samples. As originally devised by Van der Pauw, one uses an arbitrarily shaped (but simply connected, i.e., no holes or nonconducting islands or inclusions), thin-plate sample containing four very small ohmic contacts placed on the periphery (preferably in the corners) of the plate. A schematic of a rectangular VDP configuration is shown in Fig. 2.

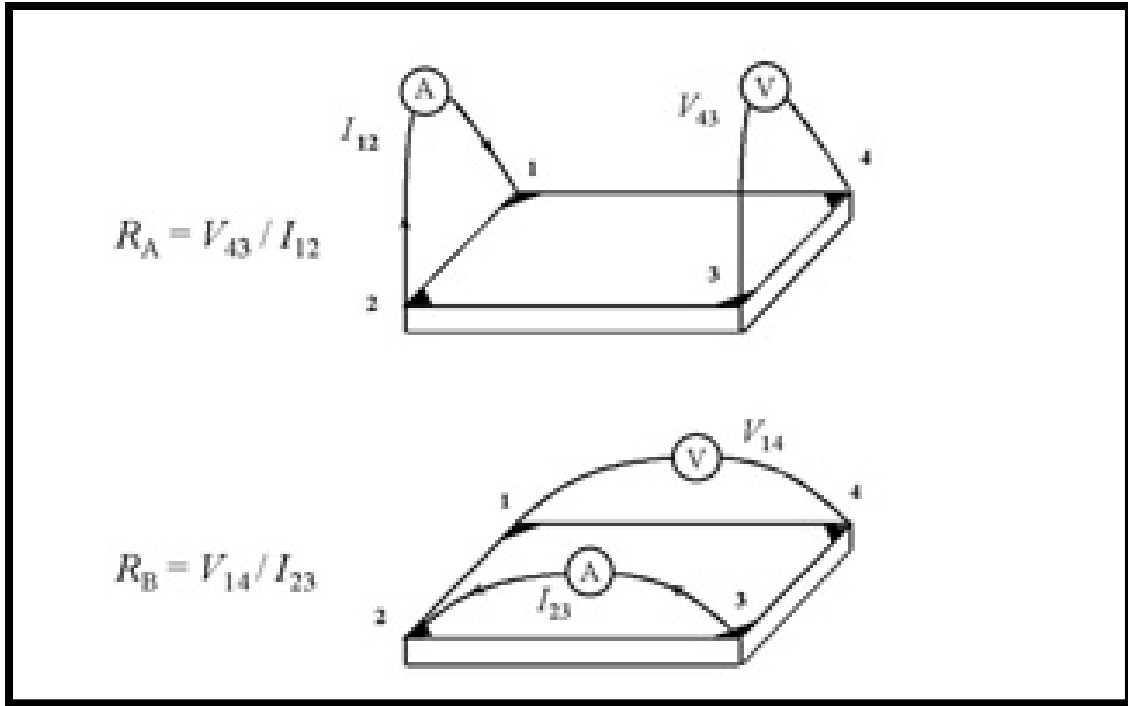


Figure 2: Van Der Pauw Technique [3]

Even though a square sample was originally used, we can consider some other configurations. Given the opportunity to take a sample from anywhere amongst the wafer, nearest the center is the choicest of locations do to the deposition uniformity. The shape of the sample and where the contacts are located is an important consideration. If achievable, the cross bridge, Figure 3,

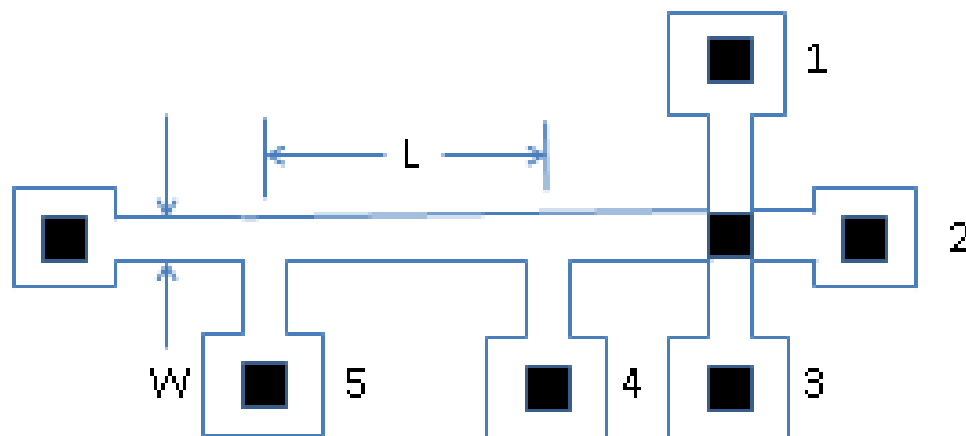


Figure 3: A Cross Bridge Sample

provides the best results for VDP measurements. But in a situation where photolithography techniques are not accessible, or need to be avoided, a cloverleaf sample is used. The practical and preferred shapes are shown in Figure 4.

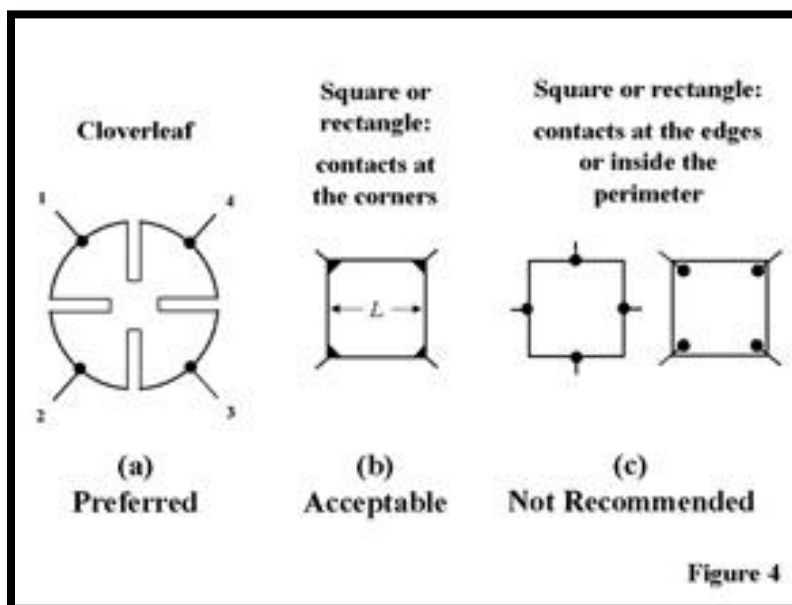


Figure 4: Preferred and Acceptable VDP Shape & Contact Configurations [3]

The cloverleaf, Figure 4(a), involves a number of delicate processing steps to accomplish which is why 4(b) is chosen because it's the easiest to achieve; also it's easily corrected for, according to D.K. Schroder [3] and Figure 5.

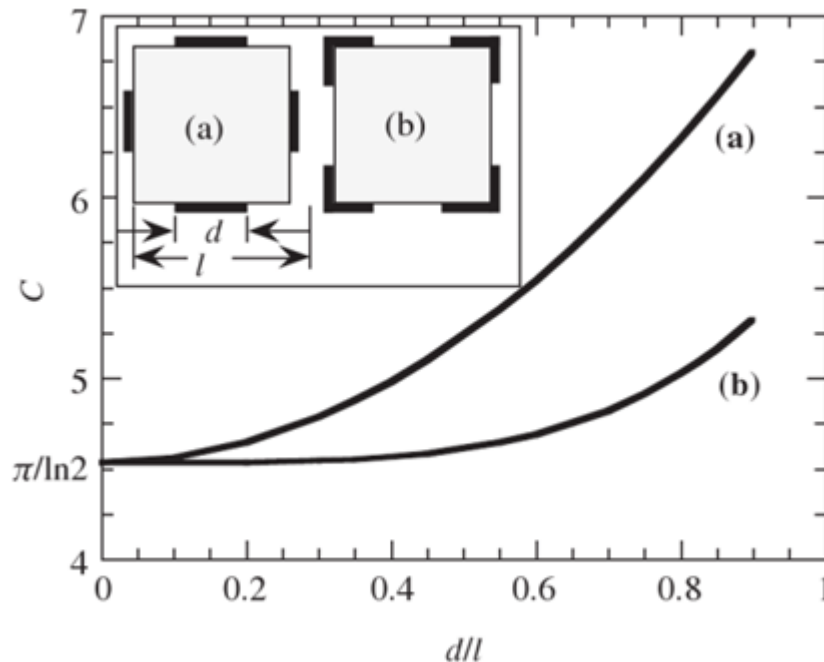


Figure 5: Correction Factor C versus d/l for contacts at the center and at the corners of the square [3].

As the ratio of the diameter of the contacts to the length of the sample side approaches zero the correction factor is multiplied by the R_{1234} as shown above in Figure 5. When d approaches l the correction factor grows exponentially as shown above.

Next the resistance measurements are carried out. With a square sample with contacts in the corners and as small as practicable the resistivity measurements are as follows:

Firstly, the IV measurements are carried out to determine the sheet resistance R_s . The procedures are:

- Apply the current I_{21} and measure voltage V_{34} .

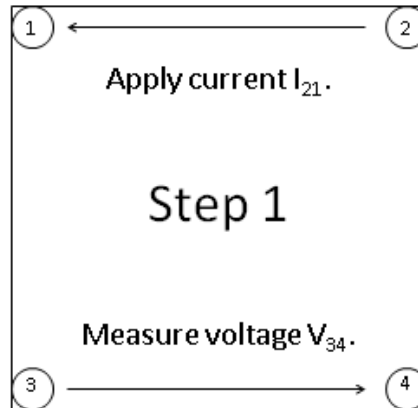


Figure 6: Measurement Demo.

- Reverse the polarity of the current (I_{12}) and measure V_{43} .

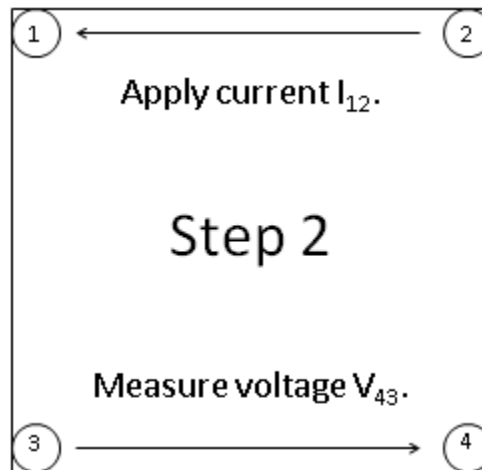


Figure 7: Reversed Current.

- Repeat for the remaining six values (V_{41} , V_{14} , V_{12} , V_{21} , V_{23} , and V_{32}).

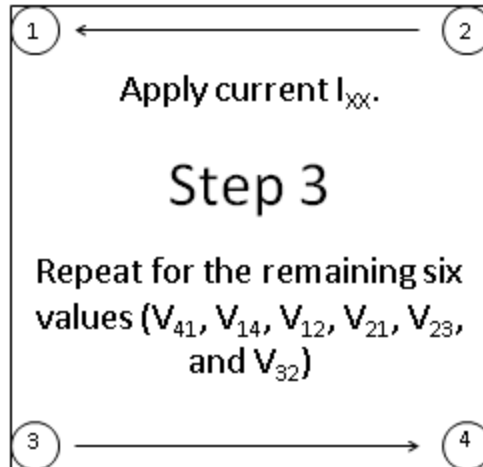


Figure 8: Remaining Six Currents.

- Eight measurements of voltage yield the following eight values of resistance, all of which must be positive:

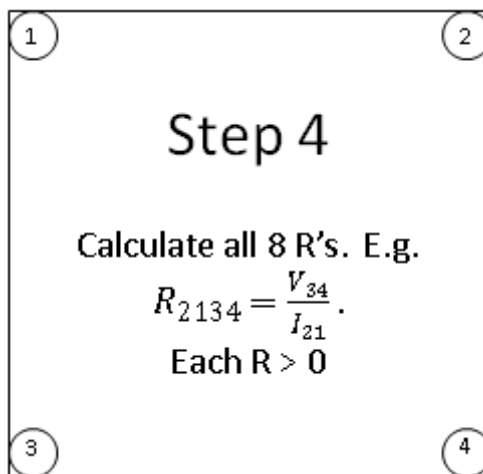


Figure 9: Calculate Resistances.

$$R_{2134} = \frac{V_{34}}{I_{21}}, R_{1243} = \frac{V_{43}}{I_{12}},$$

$$R_{3241} = \frac{V_{41}}{I_{32}}, R_{2314} = \frac{V_{14}}{I_{23}},$$

$$R_{4312} = \frac{V_{12}}{I_{43}}, R_{3421} = \frac{V_{21}}{I_{34}},$$

$$R_{1423} = \frac{V_{23}}{I_{14}}, R_{4132} = \frac{V_{32}}{I_{41}},$$

(II.24)

The redundancy is to check for consistency. The measured resistances should meet the following requirements to ensure that each contact is proportional and ohmic.

$$R_{2134} = R_{1243}, R_{3241} = R_{2314}, R_{4312} = R_{3421}, R_{1423} = R_{4132} \quad (\text{II.25})$$

$$R_{2134} + R_{1243} = R_{4312} + R_{3421}, \quad (\text{II.26})$$

$$R_{3241} + R_{2314} = R_{1423} + R_{4132} \quad (\text{II.27})$$

The experimental results must give $< 1\%$ error in equations II.25, II.26, II.27 or else the contact setups are not qualitatively similar. Two characteristic resistances R_A and R_B are defined as:

$$R_A = (R_{2134} + R_{1243} + R_{4312} + R_{3421})/4 \quad (\text{II.28})$$

$$R_B = (R_{3241} + R_{2314} + R_{1423} + R_{4132})/4 \quad (\text{II.29})$$

The sheet resistance can be numerically solved from the VDP equation:

$$\exp(-\pi R_A/R_S) + \exp(-\pi R_B/R_S) = 1 \quad (\text{II.30})$$

Now the Hall Effect measurement can be carried out.

The Hall Effect Measurement

In this section the process and math of the Hall Effect measurement will be discussed.

The process can be concisely written as the following:

- Apply the magnetic field B
- Apply a current I_{13} and measure V_{24P}
- Apply a current I_{31} and measure V_{42P}
- Apply a current I_{42} and measure V_{13P}
- Apply a current I_{24} and measure V_{31P}
- Reverse the magnetic field B

- Measure V_{24N} , V_{42N} , V_{13N} , and V_{31N} with I_{13} , I_{31} , I_{42} , and I_{24} , respectively. Four characteristic voltages are calculated by:

$$\begin{aligned} V_C &= V_{24P} - V_{24N}, & V_D &= V_{C42P} - V_{42N}, \\ V_E &= V_{13P} - V_{13N}, & V_F &= V_{31P} - V_{31N}. \end{aligned} \quad (\text{II.31})$$

If the sum of V_C , V_D , V_E , and V_F is positive, the sample is p-type. The sheet carrier concentration (cm^{-2}) is calculated by:

$$n_S = \frac{8 \cdot 10^{-8} \cdot I \cdot B}{q(V_C + V_D + V_E + V_F)}, \quad (\text{II.32})$$

Where B is the magnetic field in gauss (G) and I is the dc current in amperes (A). Then the Hall Mobility ($\text{cm}^2/\text{V}\cdot\text{s}$) is calculated by:

$$\mu_H = \frac{1}{qn_S R_S}. \quad (\text{II.33})$$

Theory of QMSA

A variety of groups have come together to develop QMSA, and make it available to the R&D community. In the magnetic field-dependent Hall Effect measurement, current I_x is applied from terminal 1 to terminal 4 on the Greek hall cross as shown in Figure 10 and a magnetic field, B_z , is applied perpendicular to the device. By measuring the voltage V_{23} between terminal 2 and 3, the resistivity ρ ($\Omega \cdot \text{m}$) is calculated by

$$\rho = \frac{E_x}{J_x} = \frac{V_{23}/d_x}{I_{14}/(d_y d_z)}. \quad (\text{II.34})$$

Where d_x and d_y are the Hall bar dimensions, d_z is the film thickness.

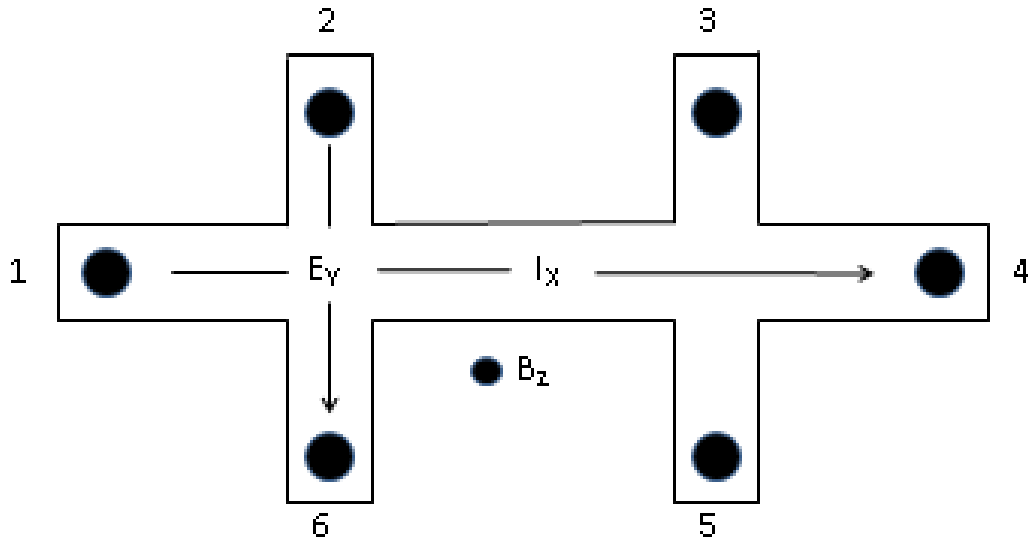


Figure 10: Greek Cross Hall-Bar Configuration.

The Hall voltage, V_Y , is measured between terminals 2 and 6, and the Hall coefficient R_H ($m^3 C^{-1}$) can be calculated by

$$R_H = \frac{E_y}{B_z I_x} = \frac{V_y/d_y}{B_z I_x/(d_y d_z)} = \frac{d_z V_y}{B_z I_x}. \quad (\text{II.35})$$

Thus the carrier concentration n (m^{-3}) and mobility μ are easily obtained from:

$$n = \frac{1}{e R_H}, \quad (\text{II.36})$$

$$\mu = -\frac{R_H}{\rho}. \quad (\text{II.37})$$

The conductivity tensor σ_{ij} ($\Omega^{-1} m^{-1}$) can be calculated from:

$$\sigma_{xx}(B) = \frac{qn\mu}{1+(\mu B)^2}, \quad (\text{II.38})$$

$$\sigma_{xy}(B) = \frac{qn\mu^2 B}{1+(\mu B)^2}, \quad (\text{II.39})$$

If the film thickness (d_z) is unknown, the sheet resistivity is measured,

$$\rho_s = \frac{d_y V_x}{d_x I_x} \left(\frac{\Omega}{sq} \right),$$

which leads to sheet carrier concentration $n_s(m^{-2})$. Then the unit of the corresponding conductivity tensor is Ω . From equations (II.22) and (II.23), the conductivity tensor can be expressed as:

$$\sigma_{xx}(B_j) = \frac{en\mu}{1+(\mu B_j)^2}, \quad (\text{II.40})$$

$$\sigma_{xy}(B_j) = \frac{en\mu^2 B_j}{1+(\mu B_j)^2}, \quad (\text{II.41})$$

where e is the electron charge, n is the sheet carrier concentration, B_j is the variable magnetic field, and μ is the electron mobility. When multiple types of carriers exist those carriers have different electron mobilities:

$$\sigma_{xx}(B_j) = \sum_k A_{xx}^{ij} [s_p(\mu_i) + s_n(\mu_i)], \quad (\text{II.42})$$

$$\sigma_{xy}(B_j) = \sum_k A_{xy}^{ij} [s_p(\mu_i) - s_n(\mu_i)], \quad (\text{II.43})$$

where,

$$A_{xx}^{ij} = \frac{1}{1+\mu_i^2 B_j^2}, \quad (\text{II.44})$$

$$A_{xy}^{ij} = \frac{\mu_i B_j}{1+\mu_i^2 B_j^2}, \quad (\text{II.45})$$

Mobility-dependent carrier density functions,

$$s_p(\mu_i) = ep(\mu_i)\mu_i, \quad (\text{II.46})$$

$$s_n(\mu_i) = en(\mu_i)\mu_i, \quad (\text{II.47})$$

As shown in equations (II.42) and (II.43), each carrier will contribute to σ_{xx} and σ_{xy} at different magnetic fields. The goal of QMSA is to extract $p(\mu_i)$ and $n(\mu_i)$ from

experimental data of $\sigma_{xx,exp}$ and $\sigma_{xy,exp}$ at different magnetic fields. In QMSA the deviation is defined as:

$$\chi_j^2 = \frac{(\Delta_{xx}^j)^2 + (\Delta_{xy}^j)^2 + (\Delta'_{xx}{}^j)^2 + (\Delta'_{xy}{}^j)^2}{N\{[\sigma_{xx,exp}^j]^2 + [\sigma_{xy,exp}^j]^2 + [\sigma'_{xx,exp}{}^j]^2 + [\sigma'_{xy,exp}{}^j]^2\}}, \quad (\text{II.48})$$

where N is the total number of mobility points, and

$$\Delta_{xx}^j = \sigma_{xx,exp}^j - \sigma_{xx}^j, \quad (\text{II.49})$$

$$\Delta_{xy}^j = \sigma_{xy,exp}^j - \sigma_{xy}^j, \quad (\text{II.50})$$

$$\Delta'_{xx}{}^j = \sigma'_{xx,exp}{}^j - \sigma'_{xx}{}^j, \quad (\text{II.51})$$

$$\Delta'_{xy}{}^j = \sigma'_{xy,exp}{}^j - \sigma'_{xy}{}^j, \quad (\text{II.52})$$

Where σ'_{xx} and σ'_{xy} are the normalized slopes defined as:

$$\sigma'_{xx}{}^j = B_j \frac{\partial}{\partial B} \sigma_{xx,exp}^j |_{B=B_j}, \quad (\text{II.53})$$

$$\sigma'_{xy}{}^j = B_j \frac{\partial}{\partial B} \sigma_{xy,exp}^j |_{B=B_j}, \quad (\text{II.54})$$

In this way QMSA will minimize the errors from $\sigma_{xx,exp}$ and $\sigma_{xy,exp}$ and at same time smooth the data fittings. The procedure includes:

- Using the Hall bar configuration, measure the V_{xx} and V_{xy} at constant current under different magnetic fields (B_j).
- Calculate the resistivity and the Hall coefficient for different magnetic fields.
- Calculate the conductivity tensor for different magnetic fields.
- Start with the first trial function (TF) to calculate χ_{sum}^2 .
- Find the mobility point which gives the lowest value of χ_{sum}^2 .

- Change the density of $p(\mu_i)$ or $n(\mu_i)$ at this mobility point and calculate χ_{sum}^2 again to check whether this change could lead to a lower value of χ_{sum}^2 .

Generally after a thousand or so iterations of the above steps, the mobility spectra with best fitting to experimental data is achieved.

Advantages of QMSA

Beyond the already mentioned ability to distinguish number, type, mobility and density of each carrier, QMSA is also the most effective tool to characterize mixed conduction devices. Modern multilayer semiconductor structures usually contain multiple populations of distinct carrier species; thus, in order to characterize a more sophisticated method such as QMSA is necessary. QMSA consists of a multi-carrier fit tool which allows the user to decide how many carriers to fit the data to and subsequently QMSA shows how well the data fits that parameter. Even more detailed information can be obtained from systematic temperature analysis of mobility spectra. By observing shifts of peaks with changing temperature and changes in their amplitude the temperature behavior of each individual carrier can be obtained [4], [5].

Because no prior assumptions are required, mobility spectrum techniques can readily identify individual carrier species occupying discrete energy levels in quantum-confined structures. QMSA has been optimized on a wide variety of wide-gap and narrow-gap III-V and II-VI bulk semiconductors, thin films, quantum wells, and multilayer device structures [6]. This extensive testing has confirmed that the optimized QMSA technique represents a convenient and universally applicable tool. It consistently shows unambiguous, accurate, and reliable results that are limited only by the quality of the input experimental data.

HEMTs are widely used and accepted as the promising components of the high-speed electronics. The mobility and sheet carrier density of the 2DEG are the most important parameters in describing the electronic properties of heterostructures and thusly QMSA is the only technique that will hastily, accurately and non-destructively characterize HEMTs [7].

III. MOLECULAR BEAM EPITAXY

Introduction

Molecular Beam Epitaxy, MBE, evolved from the work of Günther during the 1950s in which he used a “three temperature” method to grow polycrystalline, but stoichiometric films of InAs and InSb on glass substrates [8]. In his “three temperature” method he used a group V source kept at a temperature T_1 , a source of the group III-V material kept at a higher temperature T_3 , and a substrate held at an intermediate temperature T_2 . However, it was not until a decade later that Davey and Pankey demonstrated the epitaxial growth of single crystal GaAs using Günther’s method [9]. At the same time Arthur was investigating the surface kinetics of the interaction of Ga and As_2 beams with GaAs substrates which provided the basis for the understanding of the growth mechanism [10]. In the 1960s, Joyce and co-workers used a molecular beam system to investigate the nucleation of homoepitaxial Si films produced by the pyrolysis of SiH_4 [11]. They also studied the influence of the substrate surface on nucleation and the subsequent behavior of layer growth. These investigations led to the development of the MBE as a practical thin film growth technique when Cho applied a similar technique to grow thin films for device applications [12], [13], [14], [15].

MBE has advanced into many niches one of which is the study of narrow gap III-V semiconductors. These materials are grown using precise flux ratios with exact thickness determination. Using RHEED, to monitor the reciprocal lattice during the growth process the crystal structure of the growing surface and the stoichiometry can be monitored in real time.

MBE is an evaporation technique which can be used to grow thin films of high quality single crystal semiconductors. In this technique neutral atomic and molecular beams, generated thermally from heated Knudsen cells are directed onto a heated substrate under ultra-high vacuum (UHV) conditions. UHV conditions are essential to minimize the incorporation of impurities during growth [15].

Theory of MBE

Three distinguishable growth modes: layer-by-layer growth, Volmer-Weber mode, and Stranksi-Krastanov, have been established by use of statistical thermodynamics and kinetic rate equations [16], [17] and by experimental studies [18], [19].

Layer-by-layer growth through two-dimensional nucleation:

The deposited atoms or molecules are more strongly bonded to the substrate and so nucleation takes place to form monolayer islands. These islands grow to form a complete continuous monolayer. Subsequent layer growth takes place in a similar way with nucleation taking place on each completed monolayer to form islands [15].

Volmer-Weber Mode:

In which the deposited atoms are more tightly bonded between themselves than to the substrate atoms. In this case, nucleation takes place in the form of discrete three-dimensional islands on the substrate surface. These islands increase in number and size until they merge to form a continuous film.

Stranski-Krastanov Mode:

In the growth mode a finite number of monolayers are produced by two-dimensional nucleation as in (i). Subsequent growth occurs by the three-dimensional nucleation of critical size clusters as in (ii).

During MBE growth it has generally been assumed that various kinetic barriers prevent thermodynamic equilibrium from being achieved. It should be noted that the temperature of the substrate is usually different from the temperatures of the incident beams. However, the substrate temperature and the incident beam fluxes are such that there is a large overpotential for growth, in other words the rate of incorporation is faster than the rate of evaporation.

Clarke and Vvedensky examined the kinetics of MBE growth, using Monte Carlo simulations, by calculating the evolution of the surface step density [14]. Their model showed a remarkable correspondence between the evolution of the step density and the measured RHEED intensities for the specular spot during the growth of III-V semiconductors. The success of their model opened up the possibility of using such theoretical models as computer-aided design tools. This allowed for the growth of a new material to be simulated to determine the optimum growth conditions for high quality material [15].

Advantages of MBE

One of the most significant advantages of MBE is the ability to incorporate UHV-associated surface analytical equipment directly into the growth and the preparation chambers. Such equipment allows both the chemical and structural properties of the epilayers to be monitored throughout the growth process. They also aid in the optimization of growth conditions.

The growth rates in MBE are generally low: around 1 $\mu\text{m/hr}$ in other words approximately 1 monolayer per second. By using simple mechanical shutters which operate in times much less than one second, control of changes in the doping levels and alloy composition can be achieved to within atomic dimensions. The directionality of the incident beams also allows geometrical control of material structures in three dimensions by the use of simple mechanical masks. Finally since MBE is a non-thermal equilibrium growth technique, the growth of metastable alloys is possible [15].

MBE allows for homo- and heteroepitaxy. Homoepitaxy is the growth of one material onto itself. Heteroepitaxy refers to the growth of one material onto a substrate of different material, e.g. InAs on GaAs(001). MBE allows for three different ways of reducing the effects of lattice mismatch. These include:

- The growth of a buffer layer whose lattice constant is the average of the substrate and the epilayers.
- The growth of a compositionally graded buffer in which the composition and hence the lattice parameter is varied progressively from that of the substrate to that of the epilayer.
- The growth of short period strained layer superlattices.

It has been shown that strained-layer superlattices with layer thicknesses less than a critical value have led to substantial improvements in the defect density of the epilayers as compared to compositionally graded buffer layers [21].

Heterostructures

Semiconductor heterostructures are layers of two or more different semiconductors grown coherently with one common crystal structure. Heterostructures offer extra degrees of freedom in the design of semiconductor junction devices, because both the impurity doping and the conduction and valence band offsets at the junction can be controlled. Because of this freedom many devices that utilize compound semiconductors incorporate heterostructures. Examples include semiconductor lasers in CD players and high-speed devices for cell-phone systems [22].

A heterostructure may be viewed as a single crystal in which the occupancy of the atomic sites changes at the interface, or heterojunction. As an example, one side of the interface can be InGaAs and the other side GaAs with the InGaAs being strained i.e. both lattice constants are 5.65 angstroms. Both structures are built up from tetrahedral covalent bonds and fit together coherently as if they were a single crystal. If the lattice constants are such that there is relaxation of the channel, then defects and dislocations will be formed to relieve the strain energy near the interface. An example of a generic heterostructure device on silicon is represented in Figure 11.

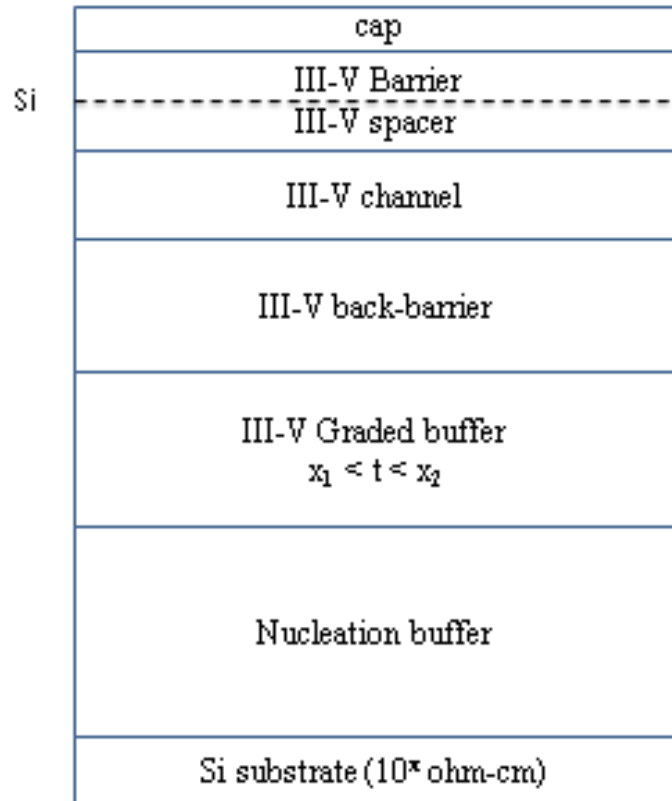


Figure 11: Generic HEMT structure.

The bandgaps, however, are different, and this difference is the source of real interest in the heterostructure, apart from the technical virtuosity in forming the structure with the channel having a smaller bandgap; the relative alignment of the conduction and valence band edges offers several possibilities such as normal, staggered and broken gap configurations. For example if Ge is used as a channel, then calculations suggest that the top of the valence band E_V in Ge should lie about 0.42 eV higher than in GaAs. The bottom of the conduction band E_C in Ge should lie about 0.35 eV lower than in the GaAs, so that the offsets are classified as normal [22].

Band edge offsets act as potential barriers with opposite effects on electrons and holes. Recall that electrons lower their energy by “sinking” on an energy band diagram,

whereas holes lower their energy by “floating” on the same diagram. For the normal alignment both electrons and holes are pushed by the barrier from the wide-gap to the narrow-gap side of the heterostructure. Some cooperative semiconductor pairs used in heterostructures are AlAs/GaAs, InAs/GaSb, GaP/Si, and ZnSe/GaAs. Good lattice matching in the range 0.1%-1.0% is often accomplished by use of alloys of different elements, which may also adjust energy gaps to meet specific device needs [22].

IV. QMSA EQUIPMENT & PROCEDURES

In this chapter the MBE and QMSA equipment that was used throughout this research is presented and described. These systems are housed in the Department of Physics at Texas State University at San Marcos, Texas.

Physical Property Measurement System

The Quantum Design Physical Property Measurement System, shown in Figure 12, has one pressure sealed, temperature controlled chamber.



Figure 12: Quantum Design PPMS Evercool Chamber.

Samples are inserted through the top using the proprietary rod which holds and releases the sample holder. The underside of the puck is where the electrical connections to the chamber are made and also prevents the sample from moving about once in the chamber.

The PPMS has an Evercool chamber, schematic shown in Figure 13, which is kept at a precise temperature, between 320-7K.

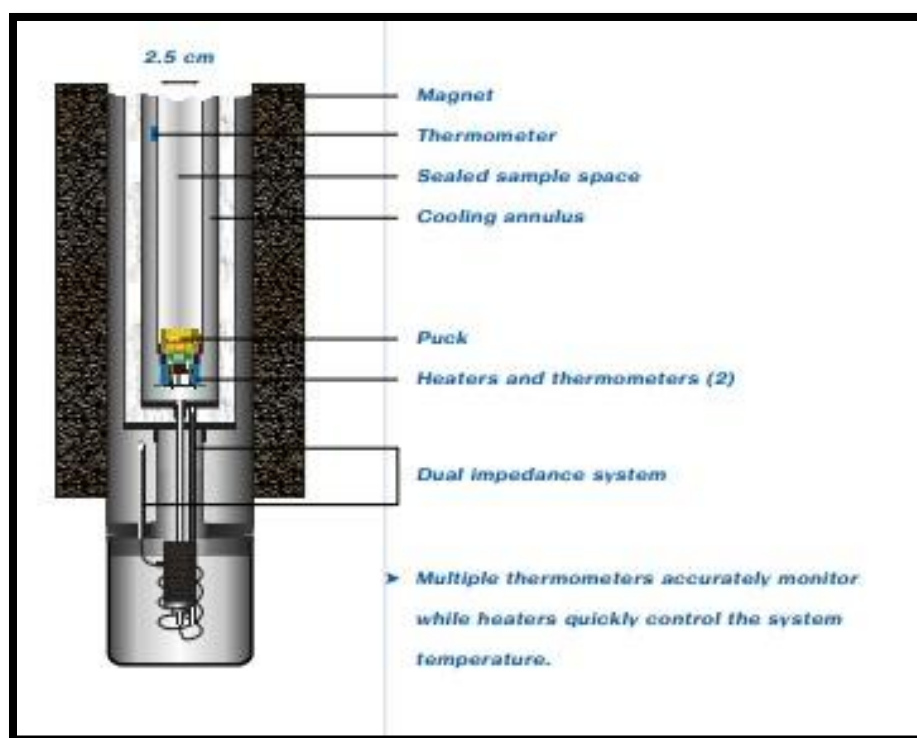


Figure 13: PPMS Inner Schematic [23].

The system is supported by a CSW-71 Helium Compressor Unit designed by Sumitomo Heavy Industries Ltd. shown in Figure 14.



Figure 14: CSW-71 Helium Compressor Unit.

As the helium heats and bleeds off it is caught, recompressed, and used to cool once again i.e. it is a closed system. The PPMS system has a Model 6700 Magnet Controller to ramp the field anywhere between 0-9 tesla. Also the electrical measurements are controlled using the Model 6500 PPMS Option Controller each of which is housed in the Quantum Design PPMS tower, as shown in Figure 15.



Figure 15: Quantum Design PPMS Tower.

The PPMS transport measurements are controlled by a PC which uses LabView to attain the specific measurements desired. LabView compiles a data file (.dat) with said values.

A Keithley 7001 Switch System digitally swaps the connections around to attain the eight VDP measurement sets.

QMSA

The QMSA analysis is administered by a program distributed by Lakeshore Cryotronics, Inc. A text file is made from the data that LabView measures and calculates. The text file is composed of: magnetic field, B (G), Hall coefficient R_H (cm^3/C), and resistivity (ohm-cm) in three columns. The text file is opened using the QMSA Analysis program. Resistivity and Hall coefficient each separately are plotted versus field (kG). The conductivity values are calculated and plotted versus field also. Then the mobilities ($\text{cm}^2/\text{V-s}$) of the existing majority and minority carriers, as many as are existent in the sample, are calculated along with their corresponding densities (cm^{-3}). Then the mobility ($\text{cm}^2/\text{V-s}$) versus conductivity (Ω^{-1}) plot is created. This plot is meaningful because it shows the majority carrier by the highest conductivity and the comparison between the different channels or carrier layers.

The InAlAs/InGaAs Si-HEMT structure grown on silicon at 300K was measured to have the 2DEG with a mobility of $8000 \text{ cm}^2/\text{V-s}$. If the 2DEG mobility peak at multiple temperatures is evaluated, an advantage of QMSA is to show how the mobility grows due to reduced temperature-dependent scattering,.

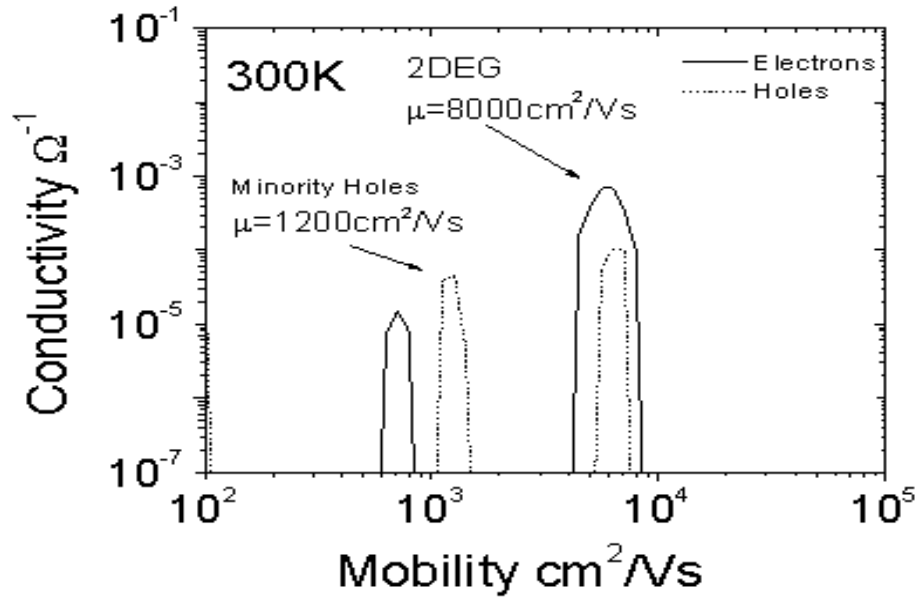


Figure 16: Mobility Peaks of Si-HEMT measured at 300K.

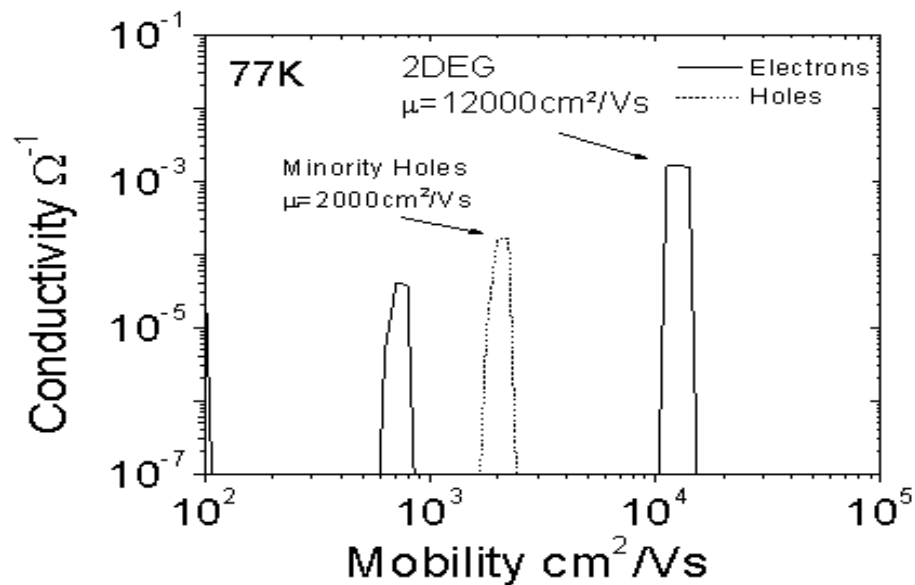


Figure 17: Mobility Peaks of Si-HEMT measured at 77K.

The smallest peak, an electron species, decreases with respect to temperature as well.

These charges come from an interface of overlapping bandgaps. The hole peak within the majority peak in Figure 16 is known as an artifact or ghost peak. It is not existent because a carrier channel will not be composed of both n and p-type carriers. The peak

furthest to the left in each plot is also considered to be an artifact for two reasons: (i) the third channel was not designed into the structure and (ii) the carrier if it exists is of such low mobility that it would be of negligible effect when in comparison to the majority and minority.

Procedure

A sample is chosen from near the center of the wafer, cleaved into a 9mm square sample. Indium contacts are soldered at about 550°C onto the sample, and in some cases annealed in a Bio-Rad Annealing Reaction Chamber for around 60 seconds at 600°C in a nitrogen atmosphere. Before VDP the contacts & sample is checked for ohmic behavior. A four point probe ohmic check is carried out in a Bio-Rad Hall Effect Measurement System. If the configuration is not ohmic the indium contacts are re-annealed until the contacts are ohmic. The contacts need to be placed in the corners of a square sample for easily correctable results [3].

For VDP measurements using the PPMS system the sample is adhered to the holder using a thin layer of rubber cement; thin enough to still be thermally conductive with the holder for the temperature control. Using a soldering iron, four gold wires are connected to the four indium contacts and tested using a digital multi-meter. Of course this step depends greatly on the sample's conducting qualities but the check is made to ensure that the wire connections are not too highly resistive and fairly equivalent to each other. If any of the connections is more than $\pm 20\%$ than the others, (i) the gold wire bonds to the indium need to be redone or (ii) contacts need better sites for congruity or (iii) the sample is too resistive due to damage from the solder iron. Once the contacts and wires are ohmic and resistively consistent, the sample is ready to be set in the PPMS

cryogenic chamber. The pressure is reduced to 10 Torr then filled with helium back to 760 Torr and then back down to 10 Torr two consecutive times to remove primarily water molecules and secondly dust in the chamber. The temperature is maintained to 300K. Before the VDP measurements a voltage vs. drive current check is carried out to find the most stable measurement current for this HEMT. A current of 10^{-5} or 10^{-6} amps is usually stable and nondestructive. The first VDP measurements are administered under the conditions: 10 Torr/300K/variable B field. The variable B field starts at 0T and moves in steps of increasing value to 8.99T. Twenty two sets of eight VDP measurements are taken over the range 0T to 8.99T. The temperature is then lowered to 77K at a rate of 5K/min, slow enough to avoid cracking the sample or loosening the adhesion. The measurements are repeated there at 77K, and finally at 10K.

V. RESULTS & DISCUSSION

In this chapter the electrical characterization of MBE grown III-V InGaAs/InAlAs heterostructures on both silicon and indium phosphide for comparison will be presented.

Structures on Si and InP

Using MBE, identical InGaAs/InAlAs HEMT heterostructures were grown on both Si and InP substrates. For the growth on the InP substrate, a buffer of a homogeneous InAlAs layer was used with an Indium composition of 52% lattice matched to the substrate. InP has a very compatible lattice constant to the HEMT device and thus doesn't require the thick graded buffer layer to realize a low defect HEMT. The structure is shown in Figure 18.

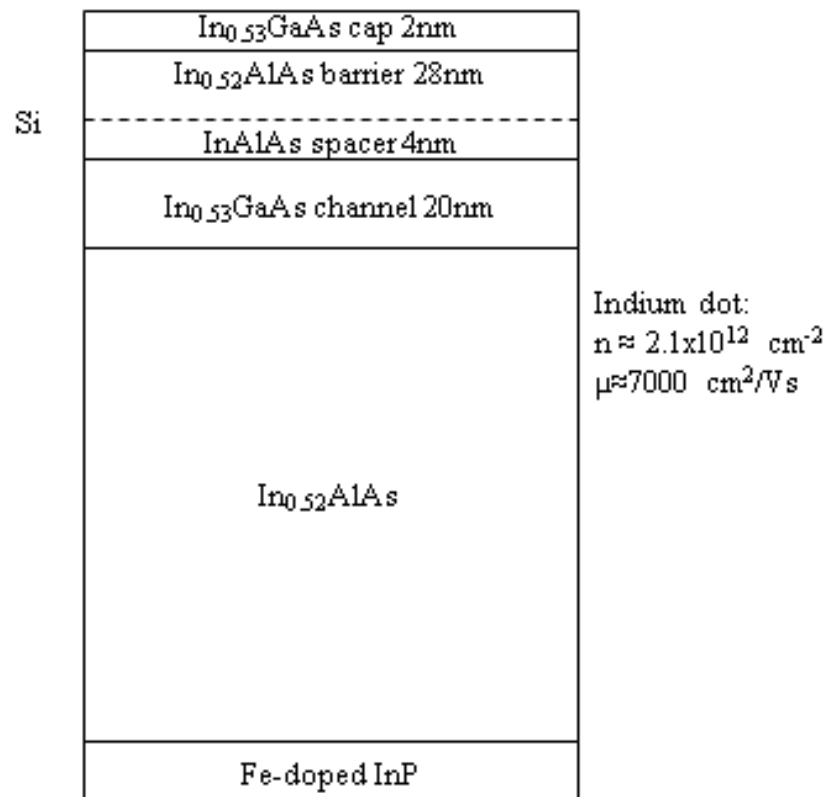


Figure 18: HEMT on InP.

On the silicon substrate a nucleation layer of GaAs was initially grown followed by a graded buffer of InAlAs in which the Indium cell temperature was increased linearly up to 52%. The channel consists of an InGaAs layer with Indium composition of 53% with a Silicon delta layer embedded in the InAlAs barrier as shown in Figure 19.

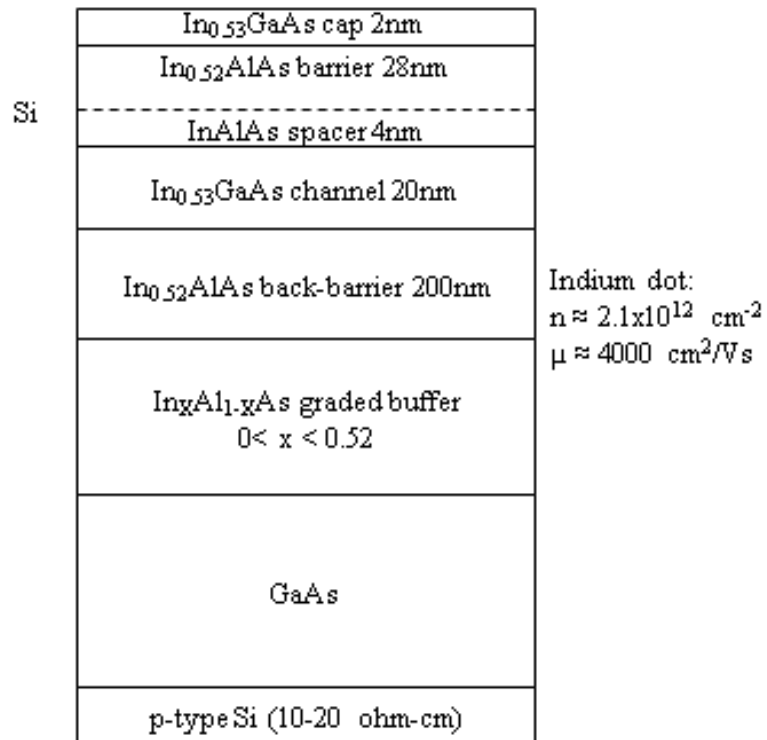


Figure 19: HEMT structure on Silicon.

The TEM in Figure 20 shows that the density of the defects due to the lattice mismatch is high close to the Si/GaAs interface with the density reducing as the thickness of the buffer layer is increased. The TEM indicates that some of the threading dislocations extend up into the channel accounting for the reduction of the mobility seen when compared to the device grown on the InP substrate.

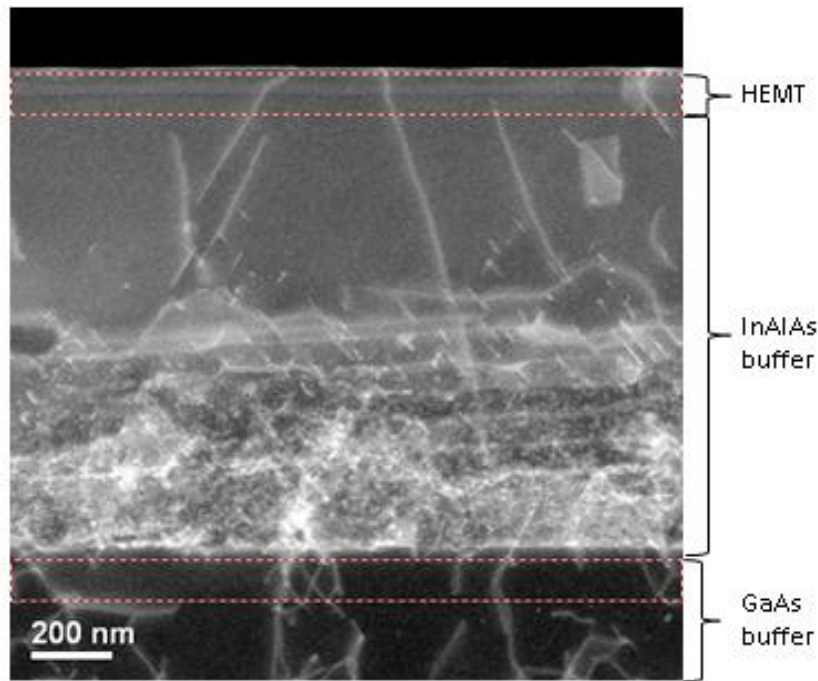


Figure 20: Cross Section TEM of HEMT-Si - x68k magnification.

The high number of defects in the lower part of the InAlAs buffer relieves lattice strain. The buffer layer for the growth of the HEMT device on Si substrates will need further optimization to decrease defects attributing to reduced mobility and conduction from species in the bulk.

It is easily seen in the TEM image an existence of threading dislocations that run from the bottom to the top of the sample. These threading dislocations can be conductive and act as local leakage paths. In a field effect transistor, these threading dislocations would increase the gate leakage current and degrade the reaction of trying to turn the device off when a negative bias on the gate becomes active. The device would not behave ideally in that it would not turn off.

Misfit dislocations are formed at mismatched interfaces via threading dislocation glide to relieve lattice mismatch. The threading dislocations react with and annihilate each other as they encounter during glide process that result in a low density of threading dislocations in the upper region of the structure where the channel resides.

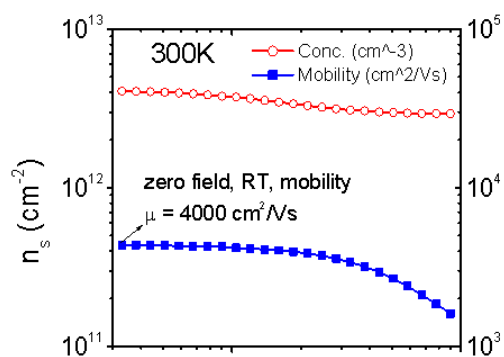
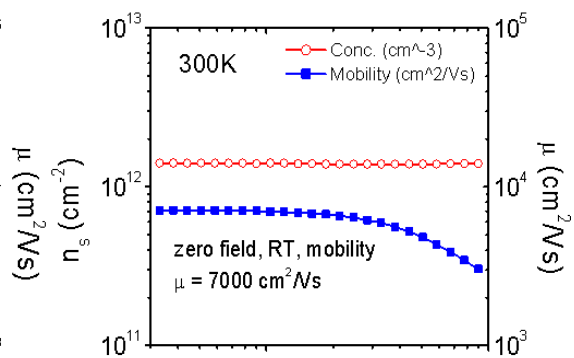
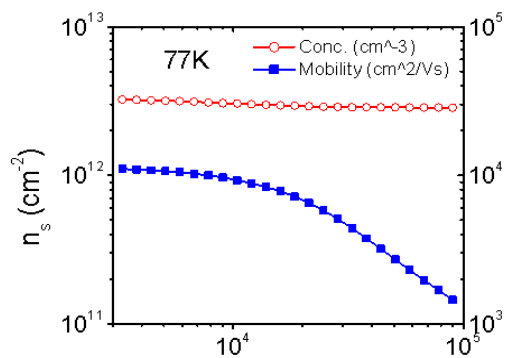
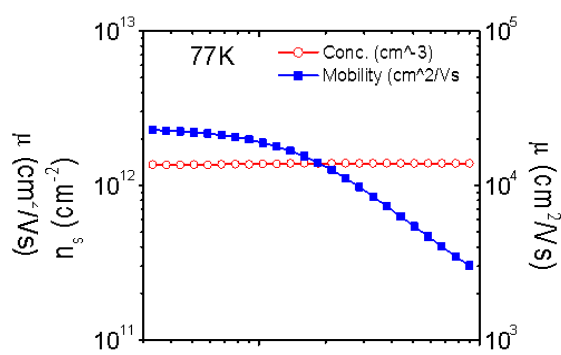
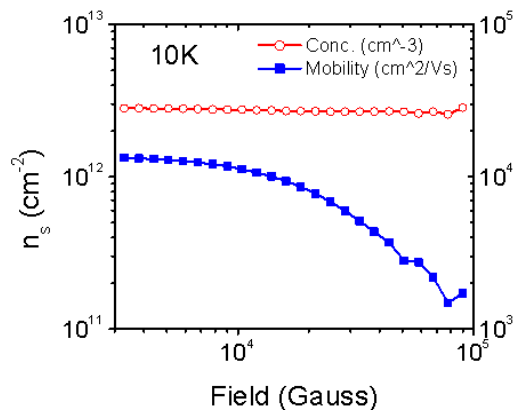
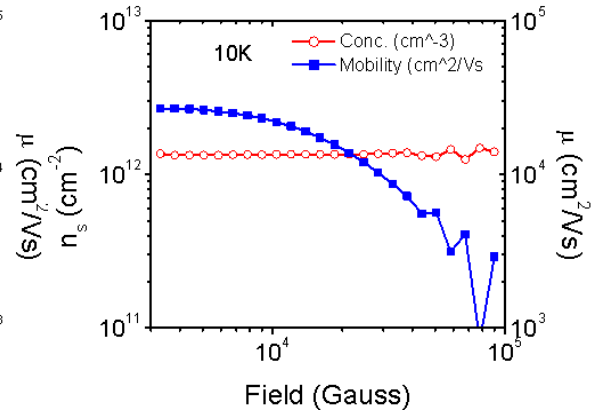
In_{0.53}GaAs/In_{0.52}AlAs on InP and Si

The HEMT on InP has virtually the same structure grown on a semi-insulating InP substrate. The measured PPMS data is used to calculate the mobility and sheet concentration then plotted versus magnetic field. This is done for each sample at each of the three temperatures. This is shown in Figures 21-26.

From the mobility versus magnetic field and the conductivity the individual species mobility plots are extracted by QMSA.

The low field 2DEG mobility are 7000 cm²/V-s and 4000 cm²/V-s for the native InP substrate and Si respectively measured at room temperature using both the PPMS and single field Hall system.. The difference is accounted for in the defects, generated by the difference in lattice constant for the case of growth on Si. The increased dislocation scattering and increased interface roughness is a result of the lattice mismatch. The difference is illustrated between Figures 27 and 28. A similar 2DEG electron peak that exists in the Si-HEMT exists in the InP-HEMT with a comparable mobility which increases as temperature decreases. For InP at 300K and 10K similar hole (dotted) peaks exist, however are absent in the 77K measurement as shown in Figures 28, 30, and 32. Even more importantly than that is the fact that there is no source of holes in the structure, meaning those peaks are most likely artifacts. These same reasons apply to the

ghost holes in the Si-HEMT structure. The ghost hole peaks are a result of the data extraction [2].

Figure 21: μ & n_s at 300K of HEMT-Si.Figure 22: μ & n_s at 300K of HEMT-InP.Figure 23: μ & n_s at 77K of HEMT-Si.Figure 24: μ & n_s at 77K of HEMT-InP.Figure 25: μ & n_s at 10K of HEMT-Si.Figure 26: μ & n_s at 10K of HEMT-InP.

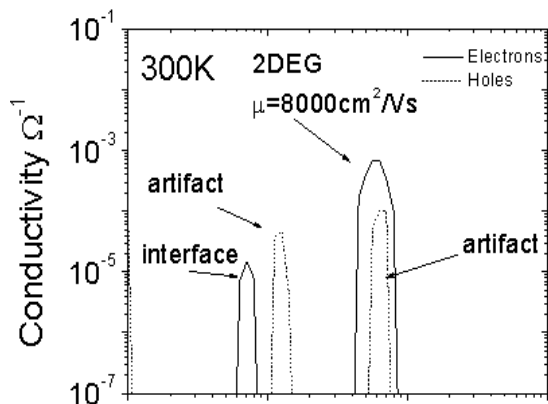


Figure 27: Mobility HEMT-Si at 300K.

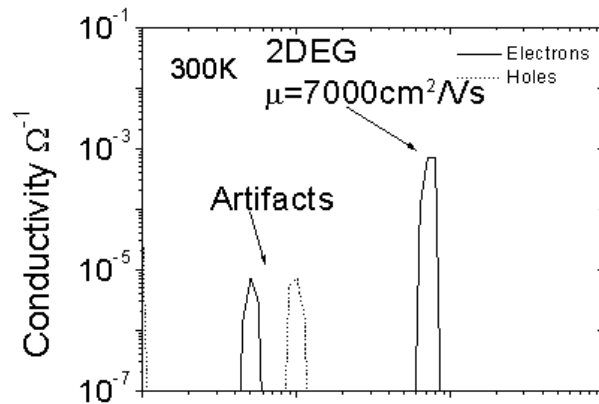


Figure 28: Mobility HEMT-InP at 300K.

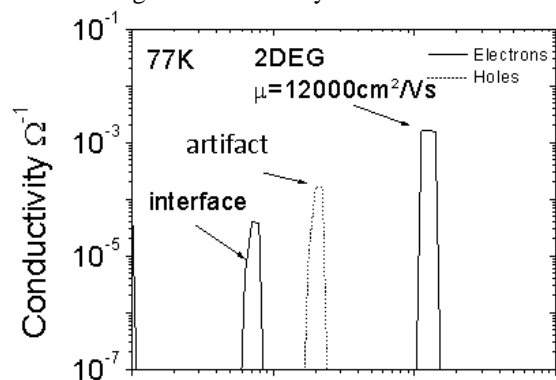


Figure 29: Mobility HEMT-Si at 77K.

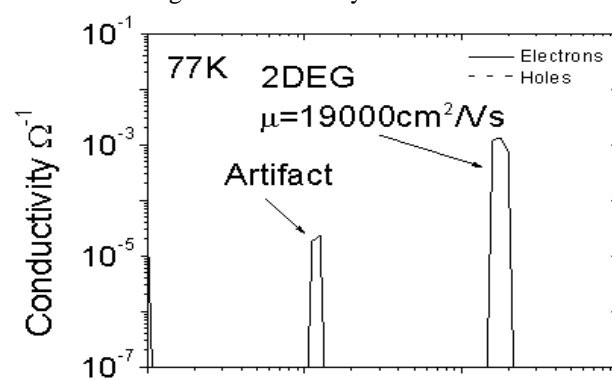


Figure 30: Mobility HEMT-InP at 77K.

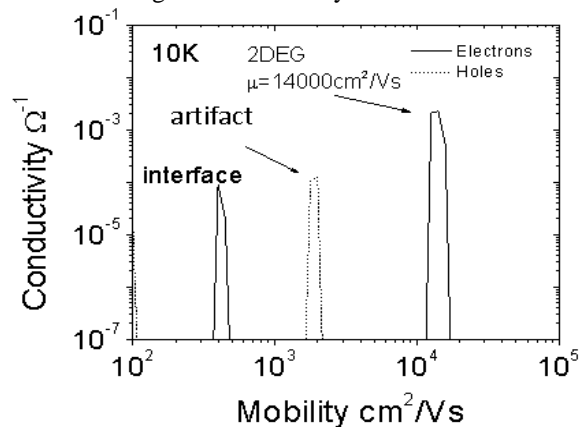


Figure 31: Mobility HEMT-Si at 10K.

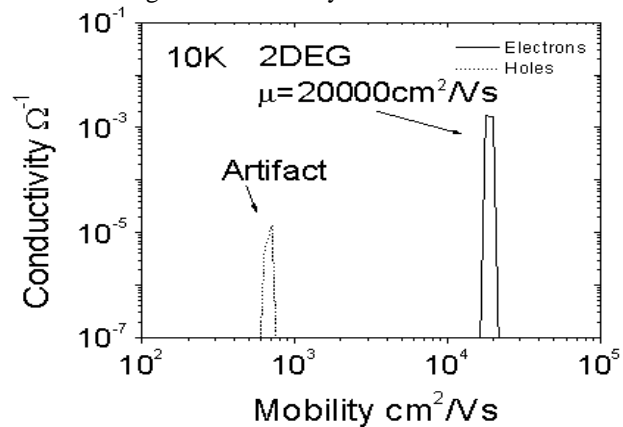


Figure 32: Mobility HEMT-InP at 10K.

The shortest electron peak has a mobility less than $1000 \text{ cm}^2/\text{Vs}$. A real low mobility channel can form at the substrate-epilayer interface due to contamination or at the silicon delta doping if the doping concentration is too high. Considering the possibility that this smallest electron peak is real it is two orders of magnitude less conductive and one order of magnitude less mobile, put simply it is negligible. This peak is likely due to degenerate parasitic conduction at the Si/GaAs interface, which may contain a high density of unintentional impurities due to prior exposure of the silicon surface to atmosphere.

The HEMT on Silicon has a large increase of mobility w.r.t. temperature due to reduced phonon scattering. When studied, the behavior of the mobility over the course of the temperature change; it is evident that the mobility increases when the temperature drops from 300K to 77K but when the temperature continues to descend the mobility becomes almost constant. The low-temperature electron mobility is limited by temperature-independent scattering mechanisms due to threading dislocations, interface roughness, and/or alloy disorder. In mixtures of elements such as InAlAs and InGaAs alloy scattering is common. Misfit and threading dislocations likely have some effect as well and were discussed and illustrated with Figure 20.

It is important to check for parasitic conduction in case the silicon doping concentration is too high or due to ionized dislocations, a second n-type conductive layer with low mobility due to parallel conduction from the silicon doping might be present [24].

Evidence of the absence of parasitic conduction may include:

1. A large conductivity ratio between the main peak (electrons in the 2DEG) and the minor peak (holes in the substrate) in a wide range of temperatures.

2. An increase in electron channel mobility with decreasing temperature.
3. A 2DEG density and mobility independent of magnetic field at different temperatures.

The mobility spectra of the two heterostructures exhibited similar features, including an expected dominant high conductivity 2DEG channel. However, the temperature-dependent carrier concentration of the HEMT-on-Si showed a decrease w.r.t. magnetic field which suggested the presence of parasitic conduction that needs to be addressed for high mobility III-V materials to be adopted for high volume manufacturing (HVM). It is likely that the conduction comes from donor impurities at the GaAs/Si interface. In the device measured, the bottom 100nm of the GaAs buffer was grown at low temperature to render it electrically insulating. Also, the InGaAs channel is grown on top of a wide bandgap InAlAs buffer. Both the low-temperature GaAs buffer and the wide bandgap InAlAs buffer should provide electrical isolation between the InGaAs channel and the GaAs/Si interface. An alternative strategy to eliminate the parasitic channel is by heavily counter-doping the GaAs/Si interface with an acceptor or amphoteric dopant to compensate the electrons.

VI. CONCLUSIONS

QMSA measurements were conducted over a wide range of magnetic fields and temperatures on MBE-grown InGaAs/InAlAs HEMT structures on Si substrates to study the impact of defects from the heteroepitaxial integration on carrier transport. Measurements from a nominally identical structure grown on a lattice-matched InP substrate were used as a reference.

The mobility spectra of the two heterostructures exhibited similar features, including a dominant high conductivity electron channel. However, the temperature-dependent carrier concentration of the HEMT-on-Si suggested the presence of parasitic conduction that needs to be addressed for high mobility III-V materials to be adopted for HVM.

DEFINITIONS

E_Y , Hall Field, electric field in the y-direction

v_x , carrier velocity in the x-direction

B_Z , z-direction magnetic field

J_X , Current density in the x-direction

n , carrier density

p , hole density

$e = 1.6 \times 10^{-19}$

R_H , Hall Coefficient

\tan , tangent

Θ_H , Hall Angle

E_X , Electric Field in the x-direction

μ_e , Electron mobility

τ , Carrier relaxation time

m^* , Effective mass

ω_c , Cyclotron frequency

r_H , Hall scattering factor

σ , Conductivity

μ_H , Hall mobility

μ , carrier mobility

dv , Change in velocity

dt , Change in time

v , Velocity of carrier

E , Electric field

B , Magnetic field

J , Electron current density

σ_{xx} , xx term of conductivity matrix

$\sigma_{xx,exp}^j$, experimental conductivity term of xx

σ_0 , Steady state conductivity

I_{xy} , Current applied between terminals x and y .

V_{xy} , Voltage measured between terminals x and y .

R_{abcd} , resistance calculated from applied current between terminals a and b , and measured voltage between terminals c and d .

R_A, R_B , characteristic voltages

R_S , Sheet resistance

V_C, V_D, V_E, V_F , Characteristic voltages

V_{24P} , Voltage measured between terminals 2 and 4 with positive current.

V_{24N} , Voltage measured between terminals 2 and 4 with negative current.

n_s , Sheet carrier concentration

q , Electron charge

ρ , Resistivity

σ_{ij} , Conductivity tensor

ρ_s , Sheet resistivity

$S_p(\mu_i)$, Hole density function

$S_n(\mu_i)$, Electron density function

A_{xx}^{ij} , Sum coefficient

χ_j^2 , Deviation of fitted values and experimental values

N, Total number of mobility points

$\sigma_{xx}^{\prime j}$, $\sigma_{xy}^{\prime j}$, Normalized conductivity slopes

$\Delta_{xx}^{\prime j}$, $\Delta_{xy}^{\prime j}$, Change between experimental and fitted normalized conductivity slopes

APPENDIX: A LIST OF PUBLICATIONS

- “Integration Challenges of III-V Materials in advanced CMOS Logic”, R. J. W. Hill, J. Huang, W. Y. Loh, T. Kim, M. H. Wong, D. Veksler, T. H. Cunningham, R. Droopad, J. Oh, C. Hobbs, P. D. Kirsch, R. Jammy. *ECS* (2012)
- “ETB-QW InAs MOSFET with scaled body for Improved Electrostatics”, T.-W. Kim, D.-H Kim¹, D.-H. Koh, R. J. W. Hill, R. Lee, M.H Wong, T. Cunningham, J. A. del Alamo², S. K. Banerjee³, S. Oktyabrsky⁴, A. Greene⁴, Y. Ohsawa⁵, Y. Trickett⁵, G Nakamura⁵, Q. Li⁶, K.M. Lau⁶, C. Hobbs, P. D. Kirsch and R. Jammy. *IEDM* (2012)

LITERATURE CITED

- [1] Gang Du, J.R. Lindemuth, B.C. Dodrill, R. Sandhu, M. Wojtowicz, Mark S. Goosky, I. Vurgaftman, J.R. Meyer. *Jpn. J. Appl. Phys.* Vol. 41 (2002) Part 1, No. 2B, 28 February 2002.
- [2] I. Vurgaftman, J.R.Meyer, C.A.Hoffman, D.Redfern, J.Antoszewski, L.Faraone, J.R.Lindemuth. *J. Appl. Phys.* 84, 4966 (1998).
- [3] D.K. Schroder, *Semiconductor Material and Device Characterization*, 3rd ed., (Wiley Interscience, IEEE Press, Hoboken, NJ, 2006).
- [4] J. Antoszewski and L. Faraone. *Opto-Electronics Review* 12(4), pp.347-352 (2004).
- [5] G.Li, J. Antoszewski, W. Xu, N. Hauser, C. Jagadish. *J. Appl. Phys.* 79, 8482 (1996).
- [6] J.R. Meyer et al. *J. Appl. Phys.* 81 (2), (1997).
- [7] S.B. Lisesivdin et al. *Appl. Phys. Lett.* 91, 102113 (2007).
- [8] K. G. Günther *Z. Naturforsch* 3a (1958) 1081.
- [9] J. E. Davey, T. Pankey *J. Appl. Phys.* 39 (1968) 1941.
- [10] J. R. Arthur Jr. *J. Appl. Phys.* 39 (1968) 4032.
- [11] B. A. Joyce Rep. *Prog. Phys.* 37 (1974) 363.
- [12] A. Y. Cho *J. Vac. Sci. Tech* 8 (1971) S31.
- [13] A. Y. Cho, H. Casey Jr. *Appl. Phys. Lett.* 35 (1974) 288.
- [14] A. Y. Cho *Jpn J. Appl. Phys.* 16 Suppl. 16-1 (1977) 435.
- [15] R. Droopad “The MBE Growth and Electrical Characterization of Narrow Gap III-V Semiconductors”. pp 12-14. (1989).
- [16]. J.W. Christian in “The Theory of Phase Transformation in Metals and Alloys” (Pergamon, Oxford) 1975.
- [17] J. A. Venables *Thin Solid Films* 50 (1978) 378.

- [18] J. D. Weekes, G. H. Gilmer *Adv. Chem. Phys.* 40 (1979) 157.
- [19] F. C. Frank, J. H. van der Merle *Proc. Roy. Soc. London A*198 (1949) 205.
- [20] S. Clarke, D. D. Vvedensky *J. Appl. Phys.* 63 (1988) 2272.
- [21] M. N. Charesse, B. Bartenlian, R. Bisaro, J. Chezelas, J. P. Hirtz *5th Euro Workshop on MBE*, Grainau, March 1989.
- [22] C. Kittel, *Introduction to Solid State Physics* 8th ed. (Wiley, Hoboken, NJ, 2005).
- [23] <http://www.qdusa.com>
- [24] N. Mukherjee et al. *Electron Devices Meeting (IEDM), 2011 IEEE International* 35.1.1 - 35.1.4.

VITA

Thiess Howard Cunningham was born at Lakenheath Air Base, Suffolk County, England, on January 24, 1988, the son of Kent Alan Cunningham and Dayna Clair Cunningham. After completing work at Wimberley High School, Wimberley, Texas, in 2006, entered Texas State University-San Marcos. Thiess received the degree of Bachelor of Science from Texas State in May 2010. During the following years was employed as a research technician with SEMATECH in Austin, Texas. In August 2010, Thiess entered the Graduate College of Texas State.

Permanent Email Address: thiess.cunningham@gmail.com

This thesis was typed by Thiess Howard Cunningham.